Journal of Controlled Release 298 (2019) 142–153

Contents lists available at ScienceDirect

Journal of Controlled Release

journal homepage: www.elsevier.com/locate/jconrel

# Mechanistic insights into the pH-dependent membrane peptide ATRAM

Vanessa P. Nguyen[a], Loganathan Palanikumar[b], Stephen J. Kennel[c], Daiane S. Alves[a], Yujie Ye[a], Jonathan S. Wall[c], Mazin Magzoub[b], Francisco N. Barrera[a,*]

[a] Department of Biochemistry & Cellular and Molecular Biology, University of Tennessee, Knoxville, TN, United States
[b] Biology Program, Division of Science, New York University Abu Dhabi, Abu Dhabi, United Arab Emirates
[c] Departments of Medicine & Radiology, University of Tennessee Medical Center, Knoxville, TN, United States

A B S T R A C T

pH-responsive peptides are promising therapeutic molecules that can specifically target the plasma membrane in the acidified extracellular medium that bathes cells in tumors. We designed the acidity-triggered rational membrane (ATRAM) peptide to have a pH-responsive membrane interaction. At physiological pH, ATRAM binds to the membrane surface in a largely unstructured conformation, while in acidic conditions it inserts into lipid bilayers forming a transmembrane helix. However, the molecular mechanism ATRAM uses to target and insert into tumor cells remains poorly understood. Here, we determined that ATRAM inserts into cancer cells with a preferential membrane orientation, where the C-terminus of the peptide traverses the plasma membrane and explores the cytoplasm. Using biophysical techniques, we determined that the membrane interaction of ATRAM is contingent on the concentration of the peptide. Kinetic studies showed that membrane insertion occurs in at least three steps, where only the first step was affected by the membrane density of ATRAM. These observations, combined with membrane binding and leakage data, indicate that the interaction of ATRAM with lipid membranes is dependent on its oligomerization state. SPECT/CT imaging in mice revealed that ATRAM accumulates in the blood pool, where it has a prolonged circulation time (> 4 h). Since fast peptide clearance and degradation in circulation are major problems for clinical development, we studied the mechanism ATRAM uses to remain in the blood stream. Using binding and transfer assays, we determined that ATRAM binds reversibly to human serum albumin. We propose that ATRAM uses albumin as a carrier in the blood stream to evade clearance and proteolysis before interacting with the plasma membrane of cancer cells. We also show that ATRAM is able to be deliver liposomes to cells in a pH dependent way. Our data highlight the potential of ATRAM as a specific therapeutic agent for diseases that lead to acidic tissues, including cancer.

## 1. Introduction

Cancer nanotechnology and nano-architectonics are being intensively studied to be used as cancer diagnosis and treatment [1,2]. It has been shown that the accumulation of nanoparticles in tumors have been improved due to the enhanced permeability and retention (EPR) effect. However, the total accumulation of nanoparticles to tumors often remains low [3]. To overcome this problem, peptides have been utilized to actively target the nanoparticles to tumor sites [4–6]. Not only do peptides improve the tumor targeting of nanoparticles, they also enhance stability [5,7]. Targeting peptides can improve the specificity and efficiency of delivery of nanoparticles and cancer drugs, as they can selectively bind to specific targets, such as cell surface receptors and ion channels [8,9]. Especially interesting are peptides able to overcome the hydrophobic core of the plasma membrane, which is a major obstacle for intracellular delivery of drugs [10,11]. The ability to fine-tune peptides according to amino acid properties allows for targeting of distinct markers and environmental triggers. For instance, de novo antimicrobial peptides (AMPs) are designed to be similar to natural AMPs. AMPs have a high overall positive charge allowing them to interact with the negatively charged lipid headgroups present in membranes of bacteria and cancer cells [12–15]. Peptides can also be rationally designed to respond to acidity. Endocytosed pH-triggered peptides can release trapped molecules, such as drugs and siRNA, from endocytic organelles as the pH of the lumen acidifies during endosomal maturation [16–19]. This is a credible way for molecules to overcome the barrier of the cell membrane and enter the cytosol. Furthermore, there are several diseases that result in an altered pH balance, such as inflammation and cancer [20–22]. The local extracellular pH of cancer cells can be 0.5–1 pH units lower than their healthy counterparts due to altered glucose metabolism, vascularization, and induction of carbonic anhydrase IX, among other factors [23–25]. *This process is accentuated by the local concentration of protons on the surface of cells, which results in a significantly more acidic pH than in the bulk microenvionment* [26,27]. Using pH-sensitive peptides as a tool to target the plasma membrane of diseased cells can allow for higher targeting specificity of acidic diseased tissues compared to healthy ones [28,29].

We have recently designed the synthetic pH-sensitive acidity-triggered rational membrane (ATRAM) peptide [30]. ATRAM is a 34-amino acid peptide (sequence:

* Corresponding author.
*E-mail address:* fbarrera@utk.edu (F.N. Barrera).

https://doi.org/10.1016/j.jconrel.2019.02.010
Received 22 October 2018; Received in revised form 28 January 2019; Accepted 8 February 2019
Available online 11 February 2019
0168-3659/ 

GLAGLAGLLGLEGLLGLPLGLLEGLWLGLELEGN) that interacts with lipid bilayers in a pH dependent manner. In neutral/basic solution, ATRAM is unstructured, but in the presence of lipid bilayers, it partitions to the membrane surface. An acidic environment causes ATRAM to insert gaining helical structure, forming a transmembrane helix, as determined by standard and oriented circular dichroism [30]. Insertion of ATRAM into the membrane is driven by protonation of the acidic glutamates, which increases the overall hydrophobicity of the peptide. Biophysical experiments showed that the membrane insertion midpoint is pH 6.5 [30]. Such pH midpoint is higher than the $pK_a$ of the Glu side chain, however this is not surprising, as the hydrophobicity of the membrane can promote large changes in $pK_a$ [31,32]. Additional *in vitro* experiments showed that ATRAM associates with melanoma and lung cancer cells more efficiently in acidic environment than at neutral pH [30]. A recent study has shown that ATRAM has a high cancer therapeutic index *in vitro* [33]. The therapeutic index was determined by comparing the efficacy of amanitin toxin labeled peptide in killing cancer cells at low and physiological pH. The higher therapeutic index indicated that ATRAM targeted cancer cells in a low pH environment more efficiently compared to a neutral pH environment. Furthermore, it also successfully targeted tumors *in vivo*, suggesting that ATRAM shows promise as a cancer therapeutics peptide [33].

To fulfill the promise of ATRAM as a therapeutic peptide, it is fundamental to understand the molecular mechanism ATRAM uses to interact with and insert into lipid membranes. Here, we determined the membrane topology by evaluation of the cellular uptake of fluorescently labeled ATRAM coupled to PEGylated liposomes. We furthermore present kinetics studies that indicate that the membrane insertion of ATRAM involves at least two intermediates. Binding and leakage experiments show that the interaction of ATRAM with lipid membranes is concentration dependent. Our results suggest that ATRAM forms oligomers at the membrane surface and the membrane interior. The degree of oligomerization importantly affects the interaction with the membrane. Renal clearance and enzymatic degradation are often challenging in therapeutic peptide design [34,35]. We investigated if this was the case, and observed that ATRAM was stable in circulation 4 h after intravenous injection. However, how ATRAM is protected from degradation and excretion is not known. We have determined that ATRAM binds to serum albumin, which we propose can explain the prolonged circulation of ATRAM in mice. The results of the SPECT/CT and biodistribution studies conducted in mice support this hypothesis.

## 2. Methods and materials

### 2.1. Preparation of liposomes

Stocks of 1-palmitoyl-2-oleoyl-sn-glycero-3-phosphocholine (POPC) and 1,2-dipalmitoyl-sn-glycero-3-phosphoethanolamine-N-(lissamine rhodamine B sulfonyl) (16:0 Liss Rhod PE) (Avanti Polar Lipids Inc., Alabaster, AL) were prepared in chloroform. Appropriate aliquots of lipids were dried with argon gas and then placed under a vacuum overnight. Unless stated otherwise, the dried lipid films were hydrated with 10 mM $NaP_i$ (pH 8.0), and large unilamellar vesicles (LUVs) were prepared with a Mini-Extruder (Avanti Polar Lipids, Inc.) through 100 nm polycarbonate filters (Whatman). For the membrane orientation studies, loaded liposomal formulation were prepared by standard physical extrusion method following the published literature [36]. In detail, lipid mixtures of POPC/POPC-FITC (75:25) and POPC/POPC-FITC/DSPE-PEG2000 maleimide (75:20:5) molar ratio were mixed in chloroform and vortexed. The solvent was evaporated using nitrogen gas, and the lipid film was left in a vacuum chamber overnight. Dry lipid was hydrated with 1 mL of 10 mM phosphate-buffered saline (PBS) (pH 7.4) to the glass vials of lipids and agitated. Hydration time was ~0.5 h with vigorous vortexing. Multilamellar liposomes were obtained after resuspension, and were subjected to 10 freeze-thaw-vortex cycles. Unilamellar liposomes were finally obtained after extruding 20 times through 100 nm polycarbonate filters. Samples were filtered before use by using a 200 nm filter.

### 2.2. Labeling of peptides

For the membrane orientation studies, DSPE-PEG2000 was conjugated at the single cysteine present at the N- or C-terminus of ATRAM (Table S1). The molar ratio between DSPE-PEG2000-maleimide (2941.605 g/mol) to ATRAM peptide (3341.95 g/mol) was approximately 1 (500 nM): 20 (1 mM). In a typical synthesis, peptide was mixed with DSPE-$PEG_{2000}$-maleimide in of methanol and stirred overnight at room temperature, and then passed through a Sephadex G-25 minicolumn (PD-10 columns; GE Healthcare Bio-Sciences, Marlborough, MA) to remove the unlabeled peptides. The size of liposomes was measured by dynamic light scattering (DLS) using a Malvern Zetasizer instrument with disposable cuvettes right after the extrusion of liposomes.

The surface charge of the liposome was – 10 mV, and size was around 175 nm (Fig. S1).

For the biophysical experiments, reactive NBD, [*N*, *N*′-dimethyl-N-(iodoacetyl)-N′-(7-nitrobenz-2-oxa-1,3-diazol-4-yl)ethylenediamine] (Thermo Fisher Scientific, Inc., Waltham, MA) was conjugated to a C-terminal cysteine in a Cys ATRAM variant and pHLIP (SI Table 1). For the cell binding assay, Y-ATRAM (Table S1) was labeled at the N-terminus with 3-BODIPY-propanoylaminocaproic acid N-hydroxysuccinimide ester (BODIPY FL-X; Invitrogen, Carlsbad, CA). In all cases, free dye was removed by gel filtration through a PD-10 column, while labeled and unlabeled peptide were separated by reverse-phase HPLC (Agilent, Santa Clara, CA). MALDI-TOF (Bruker, Billerica, MA) was used to confirm labeling.

Y-ATRAM was radiolabeled with $^{125}I$, by using chloramine T as the oxidizing agent. The reaction was quenched by addition of sodium metabisulfite. Radiolabeled ATRAM peptide was diluted in 0.1% sterile gelatin in PBS. Free radioiodine was removed through a PD-10 column equilibrated with 0.1% gelatin/PBS. Fractions containing the maximal radioactivity were collected. The product radiochemical purity was confirmed by SDS-PAGE and analyzed by phosphor imaging (Cyclone Storage Phosphor System, Perkin Elmer, Shelton, CT).

### 2.3. Cellular uptake analysis by confocal fluorescence microscopy and fluorescence-activated cell sorting (FACS)

The membrane topology of ATRAM was assessed by measuring cellular uptake with microscopy and flow cytometry. Human breast cancer MCF-7 cells (ATCC no. HTB-22) were cultured in DMEM supplemented with 10% fetal bovine serum (FBS) and 1% penicillin-streptomycin (all from Sigma) in 5% $CO_2$ at 37 °C. Once the cells reached ~ 95% confluence, they were split (using 0.25% trypsin-EDTA, Sigma) into fractions and propagated or used in experiments. Cells were seeded at a density of $2 \times 10^4$ cells/well in 500 μL complete medium in 4 well cell-view glass bottom culture dish (Greiner bio-One, Germany) for confocal microscopy or 6-well plates for FACS. After culturing for 24 h, the cells were washed and the medium was replaced with fresh phenol red- and serum-free medium (pH 6.5 or pH 7.4) containing 10 μM FITC-labeled liposomes (L), PEGylated liposomes (PL), PEGylated liposomes-ATRAM $N_t$ (PL-AN) or PEGylated liposomes-ATRAM $C_t$ (PL-AC), and incubated for 1 h. Finally, the medium was once again replaced with fresh medium to remove any extracellular liposomes. Cells were imaged on an Olympus Fluoview FV-1000 confocal laser scanning microscope, with a 63× Plan-Apo/1.3 NA oil immersion objective with DIC capability. Images were processed using the Fiji software [37]. Uptake was quantified by FACS using a BD FACSAria III cell sorter (BD Biosciences, San Jose, CA) (10,000 cells/sample, gated on live cells by forward/side scatter and propidium iodide exclusion). Analysis was performed with the BD FACSDiva software.

### 2.4. Stopped-flow fluorescence

The intermediates of the transition from the surface bound state of ATRAM to its transmembrane state was followed by stopped-flow fluorescence. Lyophilized NBD-labeled ATRAM (ATRAM-NBD) was hydrated in 10 mM NaPi pH 8.0 and incubated with POPC vesicles for 1 h at lipid-to-peptide molar ratios of 200:1, 400:1, or 600:1. The lipid-peptide samples were mixed at a 1:1 volume ratio with 100 mM sodium acetate pH 3.6 (inserted state) or 100 mM sodium phosphate pH 8 (peripheral state) to reach a final peptide concentration of 0.1 μM. Fluorescence spectra were recorded on a SX20 Stopped-Flow instrument (Applied Photophysics, Inc., Surrey, United Kingdom) with a 505 nm cut-off filter at 25 °C. The excitation wavelength was set to 488 nm. The data of the peripheral state were subtracted from the inserted state to account for potential photo-bleaching and light scattering [38]. Subtracted data were analyzed with a three-exponential model using the following equation:

$$\text{Signal} = -\text{A1} \times \exp(-k1 \times \text{x}) - \text{A2} \times \exp(-k2 \times \text{x}) - \text{A3} \times \exp(-k3 \times \text{x}) + \text{F}_\text{o} \quad (1)$$

where A is the amplitude of the signal, $k$ is the rate constant, x is time, and $F_o$ is the offset [38].

### 2.5. Sulforhodamine B leakage assay

The membrane disruption behavior of ATRAM was monitored by sulforhodamine B leakage assay in liposomes. A dried POPC lipid film was rehydrated with 20 mM sulforhodamine B (SRB) in 10 mM sodium phosphate pH 8. Large unilamellar vesicles were prepared as described above but using 200 nm filters. Non-encapsulated SRB was removed by gel filtration through a PD-10 column (GE Healthcare Life Sciences). A constant amount of peptide was added to the SRB-LUV suspensions at different initial concentrations to cover a range of peptide:lipid mole ratios. Samples with either 10 mM sodium phosphate pH 8 or 1.5% Triton X-100 were prepared as controls. After a 1-h incubation at room temperature, the pH was altered with 100 mM sodium acetate pH 4.1 or maintained with 100 mM sodium phosphate pH 7.5. The samples were measured after an additional 1-h incubation. The change in fluorescence intensity was measured using a Cytation 5 microplate reader (Biotek Instruments, Inc., Winooski, VT) with an excitation wavelength of 550 nm and emission wavelength of 590 nm. SRB leakage was calculated with the following equation:

$$\%\text{Leakage} = 100 \times \frac{(F - F_{min})}{(F_{max} - F_{min})} \quad (2)$$

where $F$, $F_{max}$, and $F_{min}$ are the measured fluorescence intensities of SRB-POPC vesicles with peptide, Triton X-100, and buffer, respectively [39].

### 2.6. NBD lipid binding assay

To determine the effect of peptide concentration on membrane affinity, the partition coefficient was determined at different peptide concentrations. Lyophilized ATRAM-NBD was hydrated in 10 mM NaPi pH 8.0 and incubated with increasing concentration of POPC vesicles at a final peptide concentration range of 0.125–0.8 μM and identical ranges of lipid-to-peptide ratio with a maximum of 500:1. The pH of the samples was changed with 100 mM sodium acetate pH 4 or 100 mM sodium phosphate pH 7.5. This was repeated with pHLIP-NBD with final peptide concentrations of 0.1375 μM and 0.55 μM. Fluorescence spectra were recorded at 25 °C with excitation at 470 nm and an emission range of 520–600 nm, using a Cytation 5 imaging plate reader. Fluorescence data (F) were normalized to the highest value of each individual isotherm and were fitted with:

$$\text{F} = \text{F}_\text{o} + \Delta\text{F} \times \frac{\text{Kp} \times [\text{L}]}{55.3 + \text{Kp} \times [\text{L}]}, \quad (3)$$

where $F_o$ is the initial fluorescence intensity, ΔF is the change between the initial and final fluorescence intensity, [L] is the lipid concentration, $K_p$ is the partition coefficient, and 55.3 is the molar concentration of water [40]. Experiments with a fitting R-squared of < 0.8 were not included due to poor fitting. All the normalized data of their respective conditions were overlaid and fitted using Eq. 2 to calculate the partition coefficient.

### 2.7. pK determination

The effect of peptide concentration on the pK of insertion was assessed by pH-titrations experiments. ATRAM-NBD was incubated with POPC vesicles at a 1:200 molar ratio and final peptide concentrations of 0.4 and 0.8 μM. The pH of the samples was adjusted accordingly with 100 mM buffers (sodium acetate, MES, HEPES, or sodium phosphate). Fluorescence emission spectra were acquired at the excitation wavelength of 480 nm. The excitation and emission slits were set to 3 nm. Measurements were performed on a Photon Technology International Quanta Master fluorometer (Edison, NJ). Appropriate lipid backgrounds were subtracted in all cases. The data were analyzed following the fluorescence intensity at 525 nm, which were then fitted to determine the $pK$, using:

$$F = \frac{F_a + F_b * 10^{m(pH-pK)}}{1 - 10^{m(pH-pK)}}, \quad (4)$$

where $F_a$ is the acidic baseline, $F_b$ is the basic baseline, $m$ is the slope of the transition, and p$K$ is the midpoint of the curve.

### 2.8. Serum albumin binding assay

To determine the possibility of ATRAM using serum albumin as a carrier molecule, a binding assay were performed. Human serum albumin (HSA, ≥96% purity, Sigma-Aldrich) and ATRAM-NBD were prepared in PBS. A constant concentration of peptide (0.4 μM) was added to a range of increasing concentrations of HSA (0.25–15 μM). The peptide concentration was chosen from the results of the lipid binding assay. The selected concentration (0.4 μM) was the lowest concentration where the peptide concentration had no effect on the partition coefficient. The concentration range of HSA was picked due to the binding curve achieving saturation. Fluorescence anisotropy was measured on Photon Technology International Quanta Master fluorometer at room temperature with the excitation and emission wavelengths set to 460 and 535 nm, respectively. The excitation and emission slits were set to 6 nm. The dissociation constant ($K_d$) was determined using the following equation:

$$< \text{r} > = < \text{r} >_b + (< r >_f - < r >_b) \frac{([\text{L}] + \text{K}_\text{d} + [\text{P}]) - \sqrt{([\text{L}] + \text{K}_\text{d} + [\text{P}])^2 - 4[\text{L}][\text{P}]}}{2[\text{P}]}, \quad (5)$$

where < r > is the measured anisotropy, < r > $_f$ and < r > $_b$ are the anisotropy for the free and the completely bound fluorescent ligand, respectively. [L] and [P] represent the total fluorescent ligand (ATRAM-NBD) and protein (HSA) concentration, respectively [41,42].

### 2.9. Vesicle transfer assay

The spontaneous transfer of ATRAM from human serum albumin to membrane vesicles was measured using a fluorescence transfer assay. Human serum albumin, POPC and ATRAM-NBD were prepared in PBS. ATRAM-NBD was incubated with POPC or HSA for 1 h with a final peptide concentration of 0.5 μM at pH 7.4. The final molar ratio of lipid to peptide was 250:1, while the molar ratio of HSA to peptide was 10:1.

Additionally, POPC was added to the samples containing the peptide-HSA mixture and incubated for 1 h. The final concentrations were kept constant. Fluorescence spectra were measured on a Photon Technology International Quanta Master fluorometer at room temperature with the excitation wavelength set to 460 nm, and the emission wavelength ranging from 490 to 630 nm. The excitation and emission slits were set to 6 nm. Anisotropy values were measured on a Horiba Fluorolog-3 spectrofluorometer (Edison, NJ) at room temperature with the excitation wavelength set to 460 nm, and the emission wavelength set to 535 nm. The excitation and emission slits were set to 6 nm. Appropriate blanks were subtracted.

### 2.10. pH-dependent cell binding

To determine whether the addition of tyrosine had an effect on the pH-dependency of the peptide in cells, pH-dependent cell binding experiments were performed with Y-ATRAM. H358 cells, obtained from ATCC, were cultured in a humidified incubator under 5% $CO_2$ in RPMI medium supplemented with 10% of Fetal Bovine Serum, 50 U/mL penicillin, 50 μg/mL streptomycin (Invitrogen). Two days prior the experiment, cells were plated at a seeding density of $1 \times 10^4$ cells per well in a 96-well black collagen-coated plate (Corning, Corning, NY). The binding assay was performed by washing cells twice with PBS supplemented with 1 mM $MgCl_2$ and 100 μM $CaCl_2$ ($PBS^{++}$) and incubating with 2 μM BODIPY labeled Y-ATRAM for 5 min. After a 90 s incubation with $PBS^{++}$ containing 10 mM dextrose (Sigma-Aldrich) at different pH values, cells were washed one time in the same pH buffer, and then fixed with 4% paraformaldehyde for 30 min. Fluorescence intensity at 488 nm was detected in a plate reader (Synergy 2, Biotek). The quantification analysis is a result of three independent experiments performed in triplicate.

### 2.11. SPECT/CT imaging

To visualize the biodistribution of ATRAM in mice, SPECT/CT imaging was performed as described elsewhere [43]. Briefly, Balb/c mice from a colony maintained at UTMC, females between 8 and 12 weeks of age, mice ($n = 3$) were injected with ~5 μg of $^{125}$I-ATRAM, ~80 μCi in the lateral tail vein. The mice were euthanized after an uptake time of either 1 h or 4 h by isoflurane inhalation overdose. SPECT images were attained using an Inveon trimodality imaging platform (Siemens Preclinical Solution, Knoxville, TN). CT data were obtained using an X-ray voltage biased to 80 kVp with a 500 mA anode current, with 4 × 4 binning. SPECT and CT images were visualized with the Inveon Research Workplace visualization software package (Siemens Preclinical Solution, Knoxville, TN).

### 2.12. Tissue biodistribution measurements

To support the SPECT/CT data, biodistribution measurements were performed as described previously [43]. Briefly, from every mouse that was imaged with $^{125}$I-ATRAM, samples of heart, kidneys, intestines, spleen, liver, pancreas, and stomach were harvested *post mortem*. Each sample was weighed, and the $^{125}$I radioactivity was measured using an automated Wizard 3 gamma counter [44] (1480 Wallac Gamma Counter, Perkin Elmer).

### 2.13. Microautoradiography

Similar to the tissue biodistribution measurements, microautoradiography was performed to support the SPECT/CT data. Each tissue sample was fixed in 10% buffered-formalin and embedded in paraffin. Then, 6-μm-thick tissue sections were dipped in NTB-2 emulsion (Eastman Kodak), stored in the dark, and developed after a 4-day exposure. Each section was counterstained with hematoxylin and eosin.

### 2.14. Peptide stability in serum

To study the stability of the peptide in serum, a concentrated stock of ATRAM-NBD (300 μM) was diluted in fetal bovine serum for different times and incubated at 37 °C. ATRAM-NBD was separated from serum proteins using chloroform/methanol, and the solvents were dried, and resuspended in methanol for HPLC. We used a StableBond Analytical Agilent Zorbax 300 SB-C18 column on an Agilent 1200 series HPLC system (Santa Clara, CA). The gradient from solvent A ($H_2O$ + 0.05% TFA) to solvent B (methanol + 0.05% TFA) started with a 15 min gradient from 5% B to 80% B followed by a 35 min gradient from 80% B to 100% B and ended with a 5 min gradient back to 5% B. Flow rate was set to 2 mL/min.

## 3. Results

### 3.1. Cellular studies of the orientation of ATRAM membrane insertion

The establishment of the TM helix of ATRAM requires only one peptide end to insert across the membrane. However, it is not known if the insertion has a preferred orientation. To determine the directionality of the membrane insertion of ATRAM, we developed an assay where either the $C_t$ or $N_t$ of ATRAM were conjugated to a large particle, which is expected to block membrane insertion through the that peptide end. Specifically, we conjugated either the $N_t$ of ATRAM (PL-AN) or the $C_t$ of ATRAM (PL-AC) separately to the PEGylated liposome (PL). We initially studied ATRAM insertion in MCF7 human breast cancer cells using fluorescence-activated cell sorting (FACS). We used fluorescent (FITC)-labeled lipids to detect any liposome attachment to the cells mediated by ATRAM. After cell incubation with PL-AN at neutral pH, most cells were not labeled, and only a small population was weakly fluorescent (Fig. 1A). However, when the experiment was repeated at pH 6.5, a pH close to the extracellular acidity of tumors [24,45], most cells were labeled and with higher intensity. Control experiments showed that use of PEGylated liposomes devoid of ATRAM (PL), or standard liposomes (L), did not induce significant labeling at either pH value (Fig. 1C). When the experiment was repeated with ATRAM conjugated with PL at the other peptide terminus, PL-AC, weak cell labeling was obtained at either pH (Fig. 1B). These results suggested that when the $C_t$ of ATRAM is available to insert into membranes (PL-AN), acidity-triggered cell insertion is observed. However, a basal insertion was also observed in all conditions when ATRAM was present. This observation suggested the presence of a secondary cellular incorporation mechanism, such as endocytosis.

Next, the cellular uptake of the liposomes (L, PL, PL-AN and PL-AC) was investigated using confocal laser scanning microscopy. FITC-labeled liposomes were visualized in MCF7 cells after incubation for 1 h at pH 6.5 or 7.4. In agreement with the FACS data, fluorescence was more intense in cells incubated with PL-AN compared to PL-AC at pH 6.5 (Fig. 1I). In both cases, the fluorescence signal was observed at the plasma membrane but also in an intracellular distribution suggesting endosomal localization (Fig. 1G). At pH 7.4, a weaker intracellular fluorescence signal was detected for both PL-AC and PL-AN (Fig. 1F, H). Taken together, the cellular results suggested that i) the C-terminal end of ATRAM inserts into cell membranes in a pH-dependent fashion, and that ii) endocytosis is a secondary nonspecific cell incorporation mechanism, albeit weaker in our experimental conditions (Fig. 1J).

### 3.2. Membrane insertion kinetics

To gain needed insights on the membrane folding and insertion pathway of ATRAM, we completed stopped-flow fluorescence kinetic experiments in vesicles, where we monitored the transition of the peptide from the peripheral state to the transmembrane state [38]. To do this, we incubated NBD-labeled ATRAM with POPC vesicles at

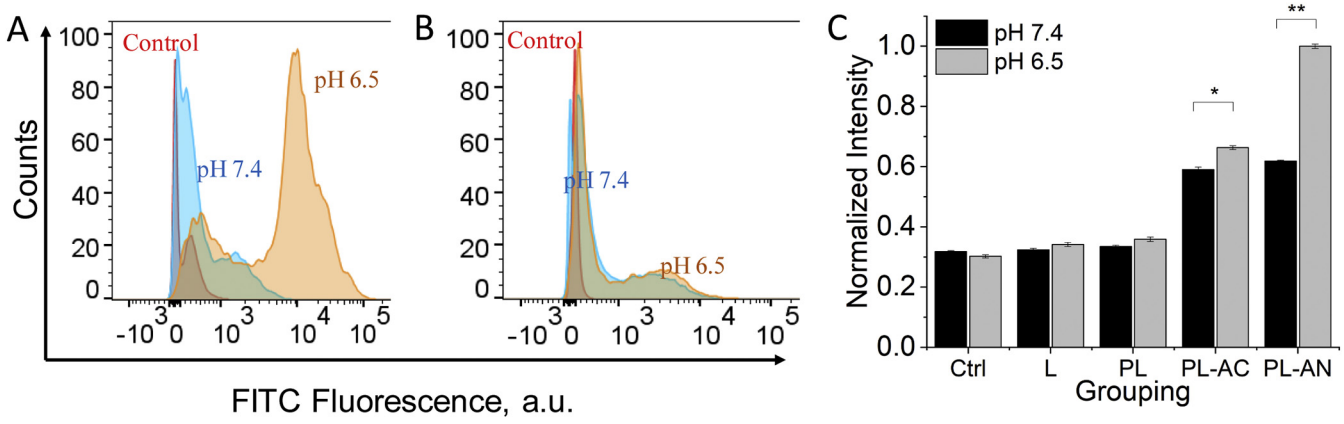


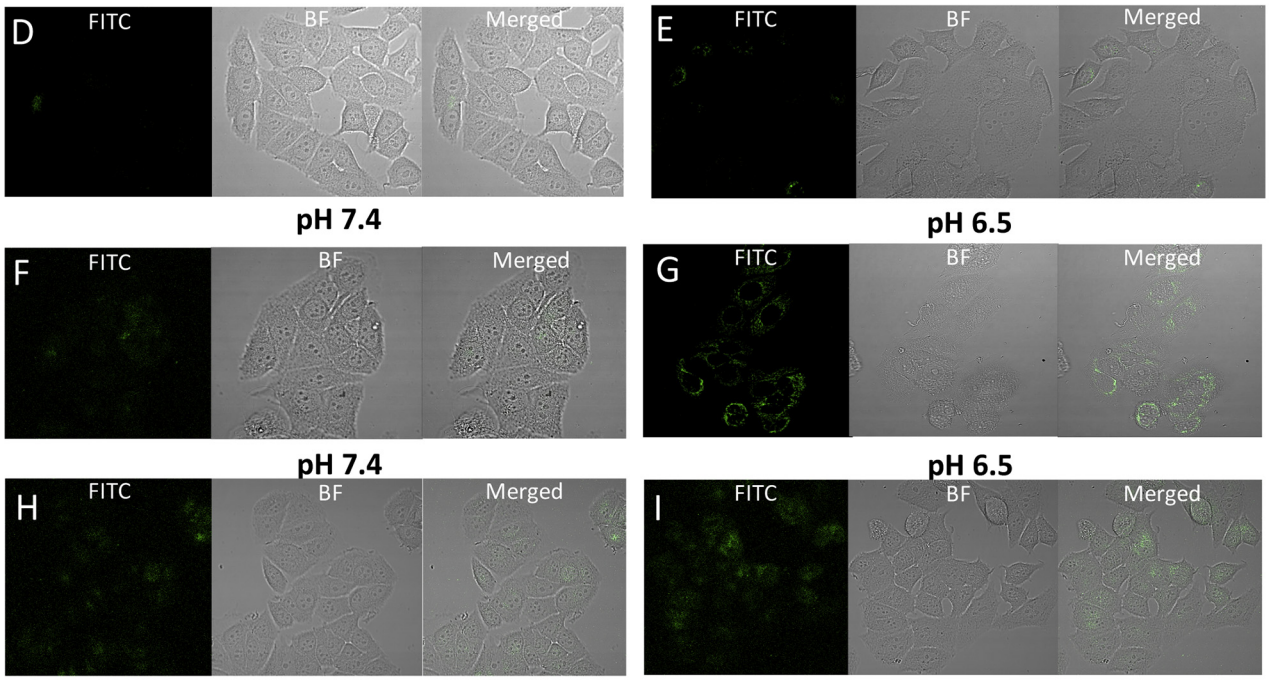


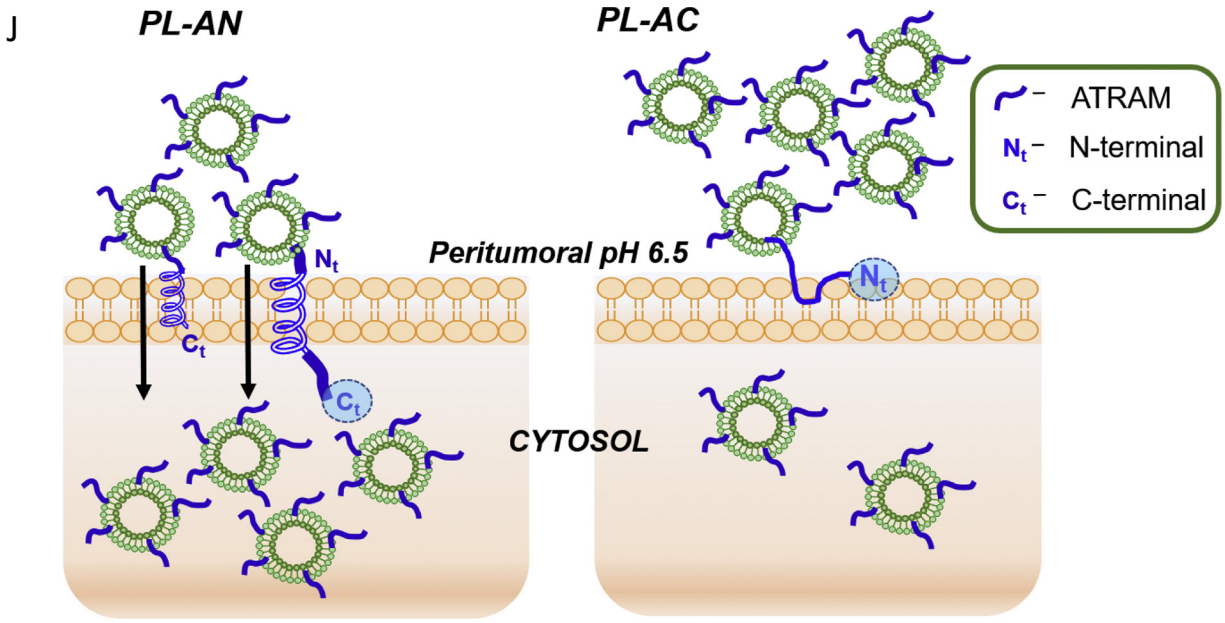


(caption on next page)

**Fig. 1.** Membrane orientation of ATRAM insertion in cells. (A-C) Quantification of cellular attachment by fluorescence-activated cell sorting (FACS). FACS analysis of MCF-7 cells treated with FITC-labeled PEGylated liposomes conjugated to (A) $N_t$ (PL-AN) or (B) $C_t$ (PL-AC) ATRAM at pH 6.5 or 7.4 were compared to background fluorescence of untreated controls. (C) Summary of the FACS data for MCF-7 cells treated with FITC-labeled liposomes (L), PEGylated liposomes (PL), PL-AC or PL-AN at pH 6.5 or pH 7.4. Mean values are shown ± S.D. Statistical analysis was carried out using the Student's t-test (n = 3). *$P < .05$; **$P < .001$ compared with their control group. (D-I) Assessment of cellular uptake by confocal fluorescence microscopy. Images of MCF-7 cells following incubation with FITC-labeled (D) liposomes or (E) PEGylated liposomes. Cells treated with FITC-labeled PEGylated liposomes conjugated to (F-G) PL-AC or (H-I) PL-AN of ATRAM at pH 7.4 and pH 6.5, respectively, 1 h. Scale bar = 10 μm. (J) Schematic description of the efficient internalization by PL-AN compared to PL-AC at the acidic peritumoral pH condition. PL-AN internalization is high, whereas the PL-AC had lower uptake. Image is not to scale and PEG is not shown.

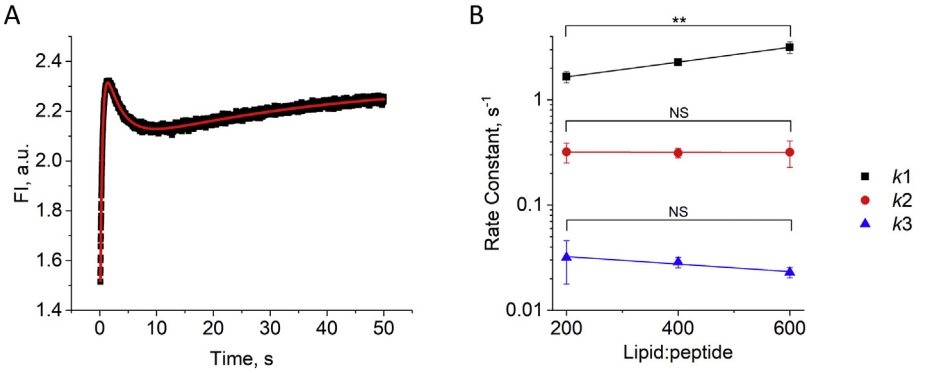


**Fig. 2.** Kinetics of ATRAM-NBD insertion in POPC bilayers. (A) Insertion of ATRAM from the peripheral to the inserted state was followed by stopped-flow fluorescence (400:1 lipid:peptide mole ratio). Curves were fitted to a three exponential model (Eq. 1), indicating at least 2 intermediates. (B) The three rate constants are shown as $k1$ (black), $k2$ (red), and $k3$ (blue). The experiment was repeated with 200:1 and 600:1 lipid:peptide mole ratios. Mean values are shown ± S.D. ($n$ = 3–4) (**, $p < .01$; NS, non-significant from ANOVA). (For interpretation of the references to colour in this figure legend, the reader is referred to the web version of this article.)

neutral pH for 1 h. Next, samples were rapidly mixed with acidic buffer (pH 4) to trigger the formation of the transmembrane state, and we followed the fluorescence intensity change of the environmentally sensitive NBD dye. We observed that the fluorescence signal increased rapidly to a maximum before decaying slightly, and then finally slowly increasing again (Fig. 2A). To establish the best fit for the stopped-flow fluorescence data, we used kinetic models with zero to two intermediate states. The two-intermediate model had the fewest intermediates that had uniform residuals (Fig. S2). This suggested that the peptide insertion process has at least two intermediate states. These stopped-flow experiments were performed at 400:1 lipid-to-peptide mole ratio. We repeated this experiment at a lower and higher lipid-to-peptide mole ratio (200:1 and 600:1).

When comparing the three rate constants, we noticed that the first rate constant was significantly affected, but not the slower second or third constant (Fig. 2B and Table S2). Thus, we observed that by decreasing the peptide density on the membrane (600:1), the first step occurred more rapidly. The peptide density here is describing the amount of available peptide for the total lipid area and does not refer to the fraction of peptide bound to the lipid. The observed density-dependence might reflect repulsion effects or changes in the oligomerization state of ATRAM. To investigate the later possibility, we performed additional biophysical studies over a range of ATRAM concentrations.

### 3.3. Membrane leakage is dependent on the oligomerization state

To gain more information about the oligomerization of ATRAM at/in the membrane, we performed a sulforhodamine B leakage assay. The assay was carried out at a constant POPC concentration and a range of ATRAM concentrations (0.00325–1.7 μM). Decreasing the lipid-to-peptide ratio from ~26,000:1 (0.00325 μM ATRAM) to 200:1 (0.5 μM ATRAM) resulted in an increase in leakage at both low and high pH (Fig. 3). However, after 200:1 lipid-to-peptide ratio at the high ATRAM concentrations, the amount of leakage decreased at both low and high pH. We also represent the leakage as function of peptide concentration (Fig. S3). We observed significant leakage (defined as > 10%), at 13 nM ATRAM and pH 8, and 52 nM at pH 4. Leakage decreased once the peptide concentration was higher than 0.5 μM. The trend of SRB leakage at pH 4 was similar to pH 7.5; it increased until ~0.5 μM, then the leakage started to decrease (Fig. S3). This showed that lower

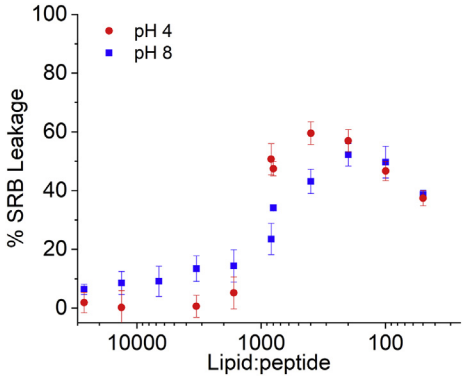


**Fig. 3.** ATRAM concentration affects POPC membrane disruption. The fluorescence intensity of sulforhodamine B (SRB) encapsulated in POPC vesicles was monitored after the addition of ATRAM (0.0025–2 mol%) at pH 7.5 (blue) and pH 4 (red). Complete leakage was achieved on addition of Triton X-100. Mean values are shown ± S.D. ($n$ = 3). Fig. S3 shows the same data presented with the concentration of ATRAM in the x-axis scale. (For interpretation of the references to colour in this figure legend, the reader is referred to the web version of this article.)

ATRAM concentrations were required for maximum leakage, while at higher concentrations, where increased ATRAM oligomerization was expected, the interaction with the membrane changed.

### 3.4. Affinity to lipid membranes is concentration dependent

The partition coefficient ($K_p$) defines the relative affinity between the solution and the bilayer phase [40]. To determine if the lipid partition coefficient of ATRAM was also contingent on peptide concentration, we performed binding experiments at two ATRAM concentrations (0.25 and 0.8 μM) at pH 4, corresponding to the transmembrane state. We observed that ATRAM bound more readily to POPC at 0.25 μM than at 0.8 μM (Fig. 4A). When we systematically repeated the binding experiments over a range of peptide concentrations (0.125–0.8 μM) (Fig. S4), we observed that at increasing ATRAM concentration, the $K_p$ decreased more than 10-fold (note the logarithmic scale in Fig. 4B) and finally leveled off around 0.5 μM. A similar decrease in affinity was also observed at physiological pH. In ideal conditions $K_p$ should not depend on the concentration of ATRAM.

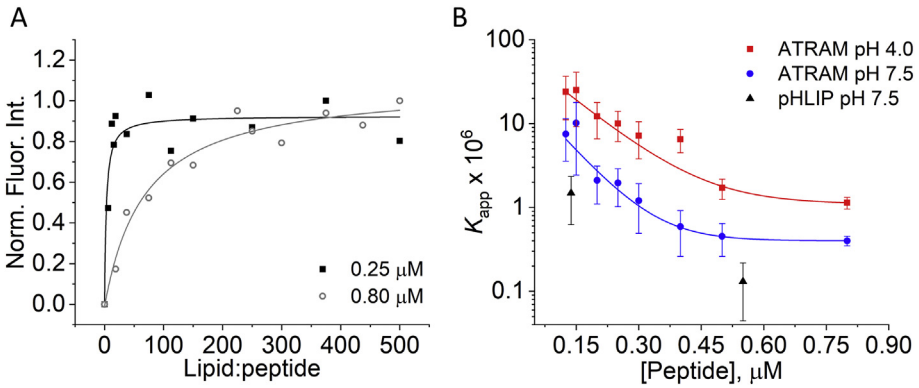


**Fig. 4.** Peptide concentration affects the adsorption of ATRAM to POPC vesicles. (A) Representative POPC binding assay of ATRAM-NBD at pH 4 with final peptide concentrations of 0.25 μM (closed symbols) and 0.8 μM (open symbols). The fluorescence intensities were normalized to the maximal value. Curves were fitted to Eq. 3 to determine the partition coefficient ($K_p$). (B) $K_{app}$ varies as a function of ATRAM concentration at both acidic (red) and physiological pH (blue), which was also observed with pHLIP at physiological pH (black). Mean values are shown ± S.D. ($n$ = 4). (For interpretation of the references to colour in this figure legend, the reader is referred to the web version of this article.)

However, as the partition coefficient is changing with concentration of the peptide, the binding is considered nonideal, and the true partition coefficient cannot be determined [40,46]. Therefore, the reported partition coefficient will be referred to hereafter as the apparent $K_p$ ($K_{app}$) [40]. As shown earlier at a single ATRAM concentration, the apparent partition coefficient was consistently higher in the transmembrane state (acidic pH) than the peripheral state (neutral pH) [30]. This result is not surprising as the four glutamates present in ATRAM would be protonated at pH 4, which increases the hydrophobicity and, in turn, the membrane affinity of the peptide. We wanted to investigate if a change in oligomerization could cause the $K_{app}$ changes observed at neutral pH. To this end we repeated the experiment with pHLIP, which is monomeric at both acidic and neutral pH under our experimental conditions. We observed that pHLIP also showed higher POPC affinity at low concentrations, indicating that a factor other than a change in oligomerization state is responsible for the $K_{app}$ changes in ATRAM. This raised the possibility that the p$K$, which reports on membrane insertion, varies at different ATRAM concentrations. To explore this possibility, we measured the pH-dependent change in the fluorescence intensities of NBD labeled ATRAM at two concentrations, 0.4 and 0.8 μM (Fig. S5). The obtained $pK$ values were 6.67 ± 0.12 and 6.66 ± 0.18, respectively. The $pK$ could not be accurately determined at concentrations lower than 0.4 μM due to poor signal. Our data suggested that oligomerization changes did not affect the steady-state pH-dependent membrane insertion of ATRAM.

### 3.5. ATRAM binds to human serum albumin

One of the biggest challenges of therapeutic peptides injected intravenously is their rapid clearance from circulation due to renal filtration and proteolytic degradation [35,47]. Notably, ATRAM is able to target tumors efficiently in mice [33]. However, it is not known how the peptide is able to evade proteolysis and clearance. We hypothesized ATRAM might avoid those processes due to being protected by binding to serum albumin. To test this possibility, we measured the change in anisotropy of NBD labeled ATRAM in the presence of human serum albumin (HSA). Upon HSA incubation, we observed a saturating increase in anisotropy, expected to result from a decrease in the tumbling rate of the HSA-bound fluorescent peptide. From the resulting isotherm, we determined that ATRAM binds to HSA with an affinity ($K_D$) of 1.13 ± 0.37 μM (Fig. 5A). This result suggested that albumin binding might be the mechanism ATRAM uses to avoid fast proteolysis and clearance in the blood stream.

Our data suggest that when ATRAM is injected into the blood stream, it can use serum albumin as a temporary carrier until it reaches its target. However, to concentrate within tumors, the peptide would need to first unbind albumin to gain access to the membrane of cancer cells. We performed a fluorescence assay to study if there was transfer of ATRAM from HSA to membranes (POPC vesicles) (Fig. 5B) [48,49]. The assay used NBD as an environmentally sensitive probe that responds to the presence of water [50,51]. The fluorescence intensity of NBD increases upon moving from a fully hydrated to a less polar environment, such as those in the HSA binding site or lipid membranes. When ATRAM-NBD binds to HSA, we observed an increase in fluorescence intensity compared to peptide in solution (Fig. 5C), which agrees with the increase in anisotropy observed in Fig. 5A. The fluorescence of NBD increased to a larger extent when the peptide was bound to POPC vesicles. The differences in fluorescence intensity of ATRAM-NBD upon binding to either POPC or HSA likely occur due to the environment of the lipid being less solvated than the HSA binding site for ATRAM. We studied next the potential transfer of ATRAM from HSA to membranes. Thus, ATRAM-NBD was preincubated with saturating levels of HSA, and then POPC vesicles were added. An increase in fluorescence intensity was observed compared to ATRAM-NBD in the presence of only HSA (Fig. 5C), which suggested that ATRAM can unbind HSA to bind vesicles. However, since the fluorescence intensity was significantly lower than ATRAM-NBD in the presence of only POPC, this suggest that a fraction of ATRAM-NBD still remains bound to HSA in the presence of POPC vesicles at neutral pH.

Additional anisotropy experiments were performed under the same conditions to confirm the findings (Fig. 5D). ATRAM-NBD in the presence of HSA had a $< r >$ value of 0.27 while in POPC vesicles the $< r >$ value was 0.19. An intermediate anisotropy was observed after POPC was added to the ATRAM-NBD/HSA sample ($< r >$ = 0.22). This confirms that ATRAM-NBD does interact with reversibly with HSA (Fig. 5E), and in our experimental conditions, a fraction of ATRAM-NBD unbinds HSA in the presence of POPC.

### 3.6. ATRAM biodistribution by imaging

Having shown that ATRAM binds to serum albumin *in vitro*, we wanted to study if it could correlate to a prolonged circulation half-life *in vivo*. Thus, we injected the peptide into wild type mice to confirm that the peptide does not undergo fast proteolysis and to study its biodistribution. To this end, a variant of ATRAM was radioiodinated with iodine-125 ($^{125}$I). Iodine-125 was incorporated into tyrosine residues under oxidative conditions [52,53]. As ATRAM does not have a tyrosine residue, we used an ATRAM variant (Y-ATRAM) where a leucine at the N-terminus was replaced with a tyrosine residue (Table S1). To ensure that the tyrosine residue does not affect the pH-responsive properties of ATRAM *in vitro*, fluorescence was used to monitor the association of BODIPY-labeled Y-ATRAM with H358 cells. After a brief incubation with the peptide, cells were rinsed with solutions of differing pH, and the fluorescence signal was evaluated. Similar to WT ATRAM, Y-ATRAM associated with cells in a pH-dependent manner with stronger interactions in acidic environments compared to neutral ones, (Fig. S6) [30], validating the use of this peptide variant.

The biodistribution of $^{125}$I-ATRAM in wild type (WT) mice was examined by SPECT/CT imaging. Fig. 6A revealed a characteristic pattern of blood pool, with high activity in the liver and heart at both 1

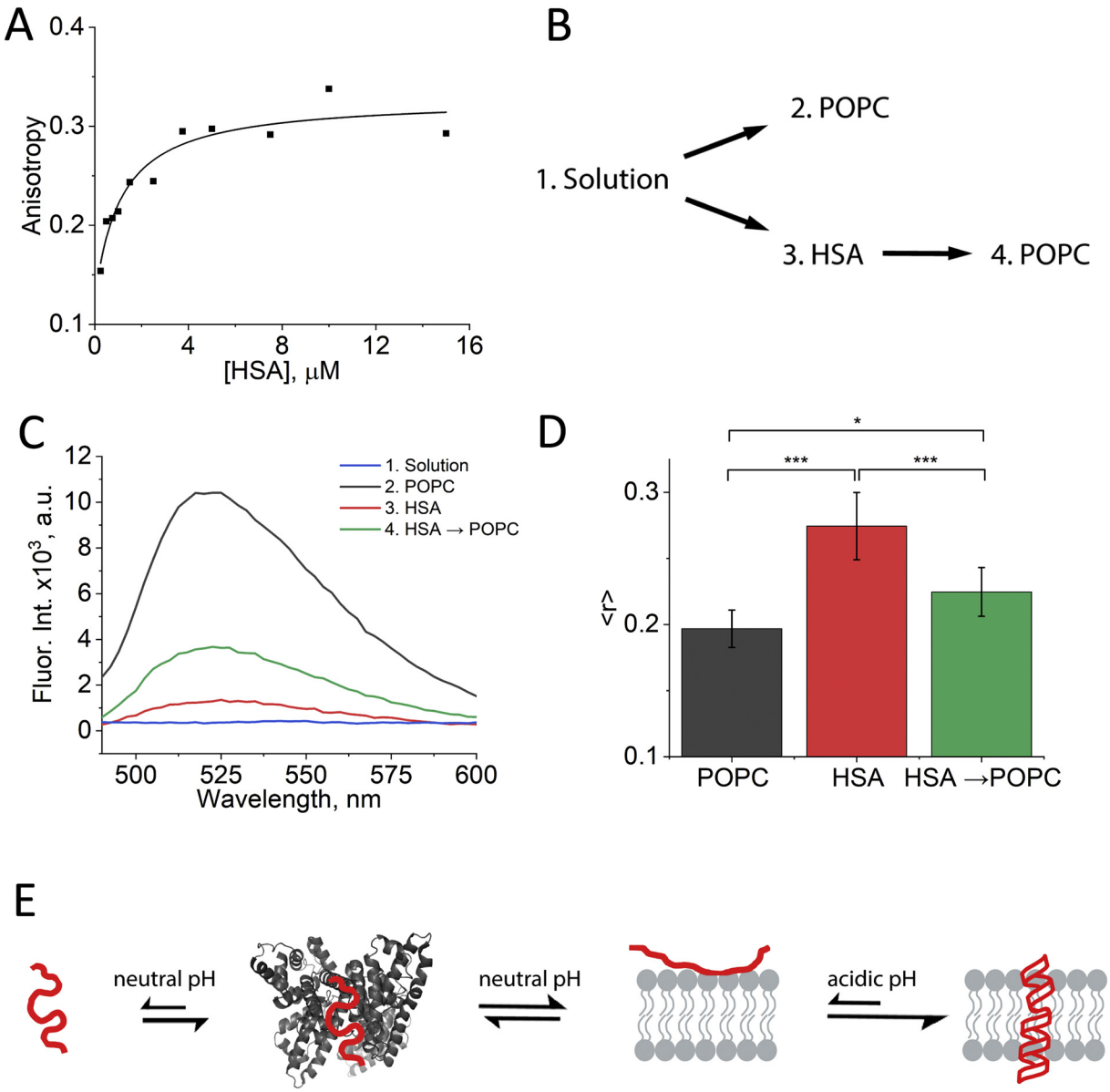


**Fig. 5.** Lipid membranes compete with human serum albumin for ATRAM binding. (A) Representative binding curve of ATRAM-NBD to human serum albumin measured by fluorescence anisotropy. The curve shows the fitting obtained with Eq. 5 to determine the dissociation constant ($K_D$). (B) Flow chart of the experimental steps to study the interaction of ATRAM with HSA and lipid vesicles. (C) Representative fluorescence spectra of ATRAM-NBD in solution (blue), bound to POPC (black), HSA (red), or bound to HSA with the addition of POPC (green). (D) Anisotropy values of ATRAM-NBD bound to POPC (black), HSA (red) or bound to HSA with the addition of POPC (green). Mean values are shown ± S.D. ($n$ = 3–4; ***, $p < .001$; *, $p < .05$ from ANOVA). (E) Model of ATRAM (red) reversibly interacting with human serum albumin (dark grey; PDB 1AO6) and lipid membranes (light grey). It is not known at which exact site ATRAM binds to HSA. Molecules are not to scale. (For interpretation of the references to colour in this figure legend, the reader is referred to the web version of this article.)

and 4 h post-injection (pi). The liver and heart were both visible 4 h pi, suggesting that there is still considerable $^{125}$I-ATRAM in the circulation. Axial views, at both time points, were taken through the plane of the liver and demonstrate intense activity in this organ that persists for at least 4 h pi. Similarly, high activity was observed in the thyroid and stomach. As radiolabeled peptide was injected intravenously, it would be eventually taken up by the kidneys and undergo catabolism and dehalogenation [54,55]. As shown in Fig. 6A, this consequently led to the sequestration of radioiodine, and thus radioactivity of the thyroid and stomach were of equivalent intensity as the liver. At 4 h pi, radioiodine levels decreased in the stomach due to emptying and gastrointestinal excretion of iodide. In contrast, the thyroid gland activity became more intense due to increased accumulation of the $^{125}$I because radioiodine is organified and will remain permanently in the thyroid [56]. Further examination indicated that there was no SPECT/CT evidence of accumulation of $^{125}$I-ATRAM at other organs and tissues. As we have shown in our biophysical experiments, lower ATRAM concentrations show higher membrane affinity and decreased membrane disruption. This could suggest that a lower concentration needs to be injected into the bloodstream to be effective.

### 3.7. *Tissue biodistribution of $^{125}$I-ATRAM radioactivity*

Tissue radioactivity measurements were performed to quantify the amount of $^{125}$I-ATRAM in various organs and tissues. Activity in the kidneys was observed, as expected, since they are the major site of protein dehalogenation in mice. Similar to the SPECT images, the liver was found to have the highest levels of radioactivity at both 1 h (18% ID/g) and 4 h (10% ID/g) pi (Fig. 6B). This suggests that $^{125}$I-ATRAM binds to components in the blood, which at some point is present at the

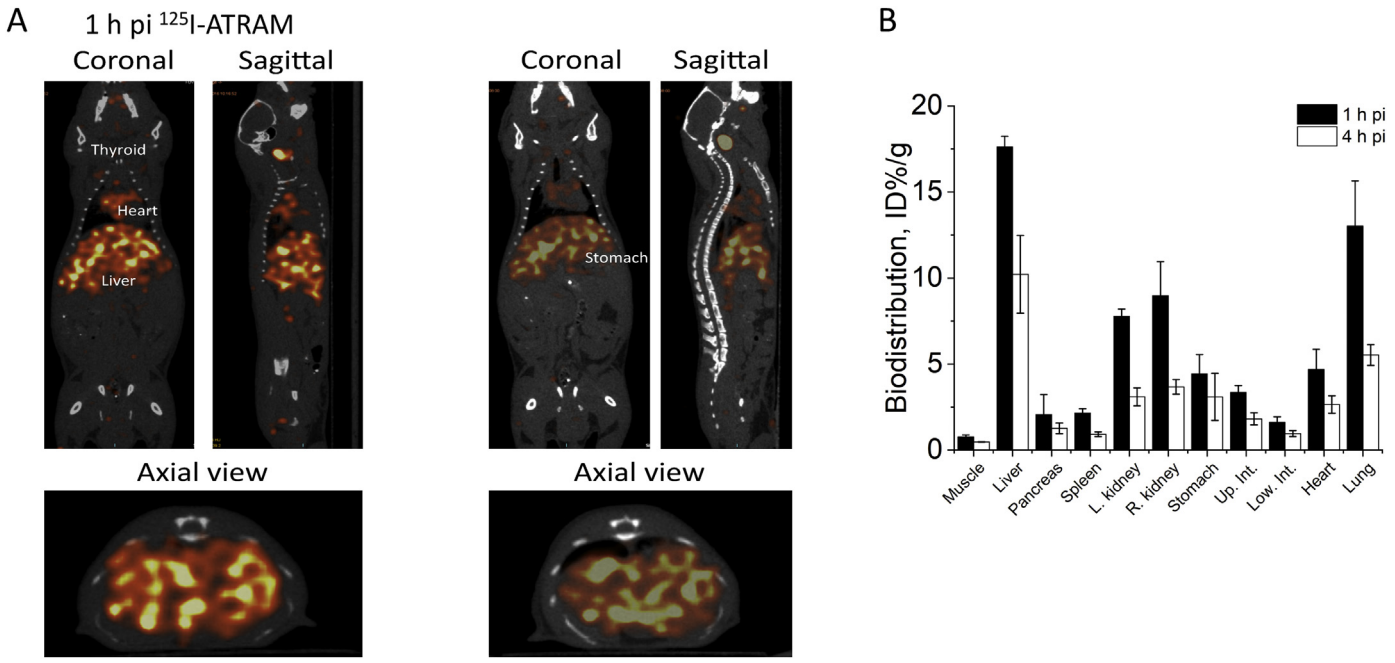


**Fig. 6.** Distribution of $^{125}$I-ATRAM mice. (A) Whole body biodistribution of radioactivity by SPECT/CT in mice injected IV at 1 h and 4 h post injection shown from the coronal, sagittal, and axial views. Radioactivity is false-colored red/yellow. (B) Tissue biodistribution of $^{125}$I-ATRAM in wild type (WT) mice at 1 h and 4 h post injection. Bars represent mean % injected dose per gram of tissue (%ID/g) ± S.D. ($n$ = 3). Up. Int., upper intestine; Low. Int., lower intestine. (For interpretation of the references to colour in this figure legend, the reader is referred to the web version of this article.)

liver. One of these components is believed to be serum albumin, since our *in vitro* data show that ATRAM binds to HSA (Fig. 5). Furthermore, albumin, the most abundant plasma protein, at a concentration of 40–50 mg/mL [57,58], is synthesized in the liver. The tissue biodistribution data also confirmed the presence and persistence of $^{125}$I-ATRAM in the heart, which represents the sum of activity in the myocardium and any blood trapped in the ventricle that was taken for tissue measurement. The spleen, pancreas, and intestines samples were all unremarkable relative to the liver, heart, and kidneys. Lungs were heavily trapped, as expected from the high levels of albumin in capillaries as well as in the pulmonary interstitium [59].

Microautoradiography was used to study the microscopic distribution of $^{125}$I-ATRAM within organs and tissues. The presence of radiolabeled peptide is evidenced by the deposition of black silver grains in the autoradiographs. Corresponding to the imaging and tissue distribution studies, there was significant accumulation of $^{125}$I-ATRAM in the liver at both time points. The distribution was not focal, suggesting that there was no accumulation within cells. The distribution appeared diffuse but intense in the sinusoids and perivascular regions (Fig. S7). The peptide was visible in the tubular lumen of the kidneys and associated with the vasculature and regions of the blood pool. In addition to evidence of $^{125}$I-ATRAM in the blood pool, there was evidence of modest levels of ATRAM in the myocardium. These organs were juxtaposed to the spleen, where little or no activity was observed at either time point. Overall, the radioisotopic studies performed in mice agree with our hypothesis that ATRAM binds to a blood component as a carrier *in vivo*, which we suggest is albumin.

Proteolytic cleavage of peptides often compromises their successful therapeutic application [60]. We hypothesized that the binding of ATRAM to albumin might provide increased resistance to proteases. To evaluate this, we studied the stability of ATRAM in fetal bovine serum (FBS) at 37 °C. We observed no noticeable peptide degradation after 17 h of FBS incubation (Fig. S8). This result might help explaining the promising biodistribution data.

## 4. Discussion

Targeted therapies have the potential to provide more effective and selective treatment for cancer. However, to fulfill this promise we first need to understand the mechanism that molecules use to attain adequate pharmacodynamics and pharmacokinetics, as well as specific targeting of diseased cells. ATRAM was designed to use the acidity prevalent in aggressive tumors [21–24] to trigger membrane insertion, which is useful for drug delivery and imaging applications [30]. ATRAM exhibits promising properties for targeting tumors [33]. In this work we carried out experiments that advanced the knowledge of the molecular basis of the action of ATRAM.

While previous studies were performed with drugs conjugated at the C-terminus of the peptide [33], it was still not known whether membrane insertion occurs through this end or if the insertion is unidirectional. With flow cytometry and microscopy studies, we have determined that ATRAM does indeed insert into cells with its C-terminus in a unidirectional fashion (Fig. 1). However, we observed partially punctate patterns of intracellular fluorescence observed in the confocal microscopy images. This is often indicative of localization to endosomal compartments, and suggests that the peptide not only is inserted at the plasma membrane but is also partly taken up by endocytosis. These studies also demonstrate that ATRAM can deliver larger molecules, in this case liposomes, to cells in a pH dependent manner.

When ATRAM is in a membrane-adsorbed state, a pH decrease induces a conformational change that results in the formation of a transmembrane α-helix [30]. However, it was not known if this process involved the presence of intermediate states. A simple two-state model cannot adequately fit the stopped-flow data shown in Fig. 2A. Instead, a triple exponential equation is required to fit the data (Fig. S2), indicating the presence of at least two intermediate states. The sign of the fluorescence intensity changes varied between different steps. A first process involved a fluorescence increase, as expected if the NBD reporter transitioned into a more hydrophobic environment. However, the second process involved an opposite intensity change. This observation suggests that the $C_t$ of ATRAM, where NBD is conjugated, temporarily explored a less hydrophobic environment. The final step

again involved a transition into a more hydrophobic environment, likely corresponding to the final formation of the transmembrane state. A similar scenario was observed for the pHLIP peptide, a monomeric pH-sensitive peptide that undergoes membrane insertion at acidic pH [28,31]. These observations suggest that pH-triggered peptides might contort into the membrane exploring different conformations before adopting the final transmembrane state [38]. Interesting insights were obtained when the stopped-flow experiment was repeated at different peptide to lipid molar ratios, which allowed us to study the effect of a change in peptide density on the surface of the bilayer. We observed that the first process was significantly faster at low peptide densities (600:1 molar lipid-to-peptide ratio). The other two processes did not show a dependency on the peptide density (Fig. 2B). However, the unambiguous identification of each process is challenging, in part because we cannot rule out that other folding steps occur within the dead time of the instrument (first ~5 ms). Nevertheless, we can hypothesize that the first step should correspond to ATRAM lying at or close to the membrane surface. If this is correct, the dependency on peptide density would suggest that in the concentration range we studied, there was a change in the oligomerization state of surface-adsorbed ATRAM. When larger oligomers are present on the membrane, this would result in a slower membrane insertion, probably because peptide-peptide interactions compete with peptide-lipid interactions.

To further probe ATRAM oligomerization, we studied if the concentration of ATRAM on the membrane surface could alter the permeability of the bilayer using an SRB leakage assay. We observed that leakage occurred at both neutral and acidic pH. The degree of leakage depended in both cases on the concentration of ATRAM (Fig. 3). This observation agrees with ATRAM forming oligomers both in the membrane-adsorbed and transmembrane states. In a recent study on aggregation of the antimicrobial peptide magainin II, Zou and colleagues found that cell membranes were disrupted less by large peptide aggregates when compared to smaller aggregates [61]. The authors propose that magainin has to overcome a high self-interaction energy before the peptide interacts with a lipid membrane. A similar behavior is proposed for ATRAM. We observed that leakage did not level off or continue to increase at ATRAM concentrations higher than 0.5 μM, but it resulted in a decrease in POPC vesicle disruption (Fig. S3). Notably, 0.5 μM is also the concentration where Wyatt et al. observed a break in the dose-dependency of ATRAM drug delivery in cancer cells [33]. The decreased in leakage shown in Fig. S3 might explain this observation, linking it to a change in ATRAM oligomerization that reduces the efficacy of drug delivery.

We previously reported that ATRAM had minimal effect on membrane leakage of a different fluorescent reporter, calcein [30]. However, in light of our current understanding of ATRAM, that study was not comprehensive enough, since it was only performed at pH 8. While the leakage results yield information on the oligomerization of ATRAM, the destabilization ATRAM induces in the lipid bilayer is not enough to cause cell toxicity, as shown by two different reports [30]. While we do not completely understand why ATRAM promotes more efficient leakage of SRB than calcein, as both molecules are similar in weight and are both anionic molecules, previous studies have shown that SRB is more prone to leakage with another peptide system [62].

We observed that the apparent partition coefficient strongly decreased (Fig. 4) at higher peptide concentrations at both low and physiological pH. To investigate the factors underlying the concentration dependency of the $K_{app}$, we repeated the experiment with NBD-labeled pHLIP. While pHLIP shows overall less affinity to bind membranes than ATRAM, at higher concentrations pHLIP also reduced its lipid affinity. As pHLIP is a monomer in the experimental conditions used, this indicates that oligomerization changes are not responsible for the $K_{app}$ changes observed for ATRAM. Instead, the dependency of the $K_{app}$ value on lipid concentration reveals that our experiments were not in infinitely dilute conditions. Thus, the pattern of specific $K_{app}$ change we obtain is characteristic of anti-cooperative partitioning, typically observed where electrostatic repulsion hinders lipid binding at high peptide concentrations. This is not surprising since both ATRAM and pHLIP have a strong negative charge (−5 and −6, respectively) in their deprotonated peripheral state [40]. For the pH 4 experiments, the peptides were incubated with POPC at pH 8 before acidification. The accumulation of negatively charged glutamates might result in electrostatic repulsion that carries into the electrically neutral transmembrane state.

Overall, our results suggest that ATRAM forms oligomers of different sizes at different membrane densities. The smaller oligomers formed at lower densities insert faster into the membrane (Fig. 2), display significantly higher membrane affinity (Fig. 4) and disrupt the membrane to a greater extent (Fig. 3) than the larger oligomers. With the increased intermolecular interaction of ATRAM, there would be a higher energy cost for the peptide to interact with the membrane, which would slow down the initial phase of membrane insertion and reduce POPC affinity. However, both oligomer sizes show similar pH-dependency of membrane of insertion (Fig. S5), suggesting that the glutamate residues that control the insertion are in similar environments [63].

Our mice data showed that ATRAM accumulates in blood-rich organs (liver and heart) (Fig. 6). Additionally, administration of the peptide did not adversely affect the test animals (data not shown). The biodistribution and SPECT/CT imaging data showed retention of radioactivity after 4 h in the heart and liver, indicating distribution throughout the circulatory system (Fig. 6). The radioactivity of $^{125}$I was still detectable in organs after 4 h, which is longer than for other peptides of comparable molecular weight [34,52,64,65]. We also observed that ATRAM was resistant to proteolytic degradation in FBS (Fig. S8). Taken together, our data indicate that ATRAM might avoid some of the biggest challenges for therapeutic peptides, as it did not undergo quick proteolysis or clearance. A possible explanation for this phenomenon is that ATRAM is transported by a blood component. In fact, strategies have been explored to prolong the half-life of peptides by increasing their affinity to serum proteins, including conjugating peptides to ligands, such as PEG and fatty acids [34,41,66–69],. Many hydrophobic molecules, such as fatty acids, cholesterol [70,71], and hydrophobic therapeutic molecules [70,72–75] are transported in the blood by binding to serum albumin, which prolongs their circulation time. Indeed, increasing albumin affinity is a common approach used to elongate the circulation half-life of biomolecules, including peptides [67,68,71]. Studies have confirmed that peptides modified with fatty acids, such as liraglutide and insulin detemir, bind to serum albumin, and as a result have a prolonged circulation half-life compared to their non-modified counterparts [68,71].

The *in vitro* data shown in Fig. 5A show that ATRAM binds to human serum albumin, suggesting that it uses this protein as a carrier in the blood stream, thereby explaining the long circulation time observed. The binding affinity ($K_D$ = 1.13 ± 0.37 μM) is slightly higher compared to a clinically used peptide, insulin detemir (4.16 μM) and other currently used drugs [71,76]. For example, phenylbutazone, warfarin, and penicillin G bind albumin with dissociation constants ranging from 1.4 μM (phenylbutazone) to 833 μM (penicillin G) [73–75]. However, a binding affinity in the micromolar scale is generally considered weak binding [77]. In our case, this could be beneficial, since too high of an affinity would preclude ATRAM unbinding HSA to target the membrane of cancerous cells. We devised an *in vitro* assay to study if this transfer could occur. We observed NBD intensity (Fig. 5C) and anisotropy (Fig. 5D) changes, indicating that ATRAM interacted with lipid membranes after pre-incubation with serum albumin. However, the partitioning away from HSA into liposomes was not complete as expected from the HSA affinity. Specifically, at neutral pH the lipid affinity of ATRAM is lower (ΔG = −7.7 kcal/mol) than for HSA (ΔG = −8.1 kcal/mol), indicating that ATRAM favors HSA. Furthermore, it has been shown before that HSA interacts with lipids [78–80]. This raises the possibility that ATRAM might be directly transferred

from HSA to POPC, forming a ternary complex under the experimental conditions of Fig. 5C–D. Based on the low affinity of HSA to DMPC lipid vesicles ($K_D$ = 6.7 mM), only ~3.5% of HSA would be bound to the lipid vesicles [81]. As a result, we expect that ATRAM must be in solution before binding to lipid vesicles.

In the experimental conditions of Fig. 5C–D, we worked with $4.2 \times 10^{14}$ HSA molecules, and a significantly larger number of POPC molecules, $2.1 \times 10^{16}$, which could be erroneously interpreted as a larger affinity for HSA than POPC. However, the interaction of a peptide with lipids should not be considered as a chemical equilibrium. Instead, it is more appropriate to consider the interaction with the whole liposome surface [40]. Based on the size of the liposome and the POPC area per lipid, we calculated that in our experimental conditions, the number of POPC liposomes was only $2.6 \times 10^{11}$, a number significantly smaller than the number of HSA molecules. Within the limitations of our *in vitro* conditions, we consider the excess of HSA over the bilayer surface might not be too far away from the situation an HSA-bound ATRAM faces in the interior of a vein or capillary, where it would slowly partition into cells. Our results suggest that ATRAM could use HSA as a carrier and protector to travel through the bloodstream. At this point, ATRAM can potentially unbind HSA to migrate into the plasma membrane of cancer cells.

Here we start to unravel the molecular mechanism ATRAM uses to target tumors. Achieving this ambitious goal requires understanding not only the mechanism of specific insertion in acidic membranes, but also the processes that allow for satisfactory biodistribution. However, in order to make ATRAM a strong therapeutic candidate, other key parameters need to be determined. To understand the insertion mechanism of ATRAM, the different oligomerization states of the peptide should be further characterized. We hypothesize that the reason ATRAM can assemble into different oligomers might be the presence of several GxxxG motifs, which often promote self-assembly of transmembrane domains [82,83].

To advance the field of therapeutic peptides, the properties of targeted peptides, such as ATRAM, need to be further understood. This is required to optimize some off-target localization and the pH profile of ATRAM, which are currently under investigation in our laboratory. Here, we were able to gain new biophysical insights into the pH-dependent membrane interaction of ATRAM. We also showed that ATRAM can deliver PEGylated liposomes to breast cancer cells in a pH-dependent fashion. We hypothesize ATRAM can target to the acidic microenvironment of tumors a wide range of nanoparticles, with probably the exception of positively charged nanoparticles, which might stablish deleterious electrostatic interactions with the charged glutamates in ATRAM. Furthermore, we also discovered that ATRAM interacts with a plasma protein, serum albumin, which might explain its promising biodistribution in mice. Different types of blood proteins bind to the surface of nanoparticles, forming a so-called protein corona [84]. The protein corona is an important determinant of the specificity and efficiency for the uptake of nanoparticles. Our results strongly suggest that ATRAM-decorated nanoparticles will contain albumin in the inner layers of the corona. This might be a desirable property, since the ATRAM-albumin affinity is weak, and this might preclude the formation of a stable “hard” corona [85]. Overall, our studies provide new insights necessary to develop ATRAM for direct targeting of drugs to cells with an altered pH environment, such as tumors.

## Acknowledgements

We are thankful to the members of Barrera laboratory for discussions and comments. We thank Dr. Dan Roberts for the use of their stopped-flow instrument. This work was partially supported by National Institutes of Health grantsR01GM120642 to F.N.B. and R01DK079984 to J.S.W., and grant AARE17-089 to M.M.

## Appendix A. Supplementary data

Supplementary data to this article can be found online at https://doi.org/10.1016/j.jconrel.2019.02.010.

## References

[1] M. Komiyama, K. Yoshimoto, M. Sisido, K. Ariga, Chemistry can make strict and fuzzy controls for bio-systems: DNA Nanoarchitectonics and cell-macromolecular, Nano 90 (2017) 967–1004.
[2] J. Shi, P.W. Kantoff, R. Wooster, O.C. Farokhzad, Cancer nanomedicine: progress, challenges and opportunities, Nat. Rev. Cancer 17 (2017) 20–37.
[3] A.M. Sofias, T. Andreassen, S. Hak, Nanoparticle ligand-decoration procedures affect in vivo interactions with immune cells, Mol. Pharm. 15 (2018) 5754–5761.
[4] F. Rinaldi, P.N. Hanieh, E. Del Favero, V. Rondelli, P. Brocca, M.C. Pereira, O.A. Andreev, Y.K. Reshetnyak, C. Marianecci, M. Carafa, Decoration of nanovesicles with pH (low) insertion peptide (pHLIP) for targeted delivery, Nanoscale Res. Lett. 13 (2018) 391.
[5] C.D. Spicer, C. Jumeaux, B. Gupta, M.M. Stevens, Peptide and protein nanoparticle conjugates: versatile platforms for biomedical applications, Chem. Soc. Rev. 47 (2018) 3574–3620.
[6] Z.E. Hughes, M.A. Nguyen, Y. Li, M.T. Swihart, T.R. Walsh, M.R. Knecht, Elucidating the influence of materials-binding peptide sequence on Au surface interactions and colloidal stability of Au nanoparticles, Nanoscale 9 (2017) 421–432.
[7] Q. Zou, M. Abbas, L. Zhao, S. Li, G. Shen, X. Yan, Biological photothermal nanodots based on self-assembly of peptide–porphyrin conjugates for antitumor therapy, J. Am. Chem. Soc. 139 (2017) 1921–1927.
[8] K. Fosgerau, T. Hoffmann, Peptide therapeutics: current status and future directions, Drug Discov. Today 20 (2015) 122–128.
[9] C. Recio, F. Maione, A.J. Iqbal, N. Mascolo, V. De Feo, The potential therapeutic application of peptides and peptidomimetics in cardiovascular disease, Front. Pharmacol. 7 (2016) 526.
[10] S.R. Hughes, P.F. Dowd, E.T. Johnson, Cell-penetrating recombinant peptides for potential use in agricultural pest control applications, Pharmaceuticals 5 (2012) 1054–1063.
[11] A. Falanga, M. Galdiero, S. Galdiero, Membranotropic cell penetrating peptides: the outstanding journey, Int. J. Mol. Sci. 16 (2015) 25323–25337.
[12] M.M. Javadpour, M.M. Juban, W.-C.J. Lo, S.M. Bishop, J.B. Alberty, S.M. Cowell, C.L. Becker, M.L. McLaughlin, De novo antimicrobial peptides with low mammalian cell toxicity, J. Med. Chem. 39 (1996) 3107–3113.
[13] B. Deslouches, S.M. Phadke, V. Lazarevic, M. Cascio, K. Islam, R.C. Montelaro, T.A. Mietzner, De novo generation of cationic antimicrobial peptides: influence of length and tryptophan substitution on antimicrobial activity, Antimicrob. Agents Chemother. 49 (2005) 316–322.
[14] N. Papo, Y. Shai, Host defense peptides as new weapons in cancer treatment, Cell Mol. Life Sci. CMLS 62 (2005) 784–790.
[15] B. Deslouches, Y.P. Di, Antimicrobial peptides with selective antitumor mechanisms: prospect for anticancer applications, Oncotarget 8 (2017) 46635–46651.
[16] E. Mastrobattista, G.A. Koning, L. van Bloois, A.C. Filipe, W. Jiskoot, G. Storm, Functional characterization of an endosome-disruptive peptide and its application in cytosolic delivery of immunoliposome-entrapped proteins, J. Biol. Chem. 277 (2002) 27135–27143.
[17] K. Kusumoto, H. Akita, S. Santiwarangkool, H. Harashima, Advantages of ethanol dilution method for preparing GALA-modified liposomal siRNA carriers on the in vivo gene knockdown efficiency in pulmonary endothelium, Int. J. Pharm. 473 (2014) 144–147.
[18] J. Wolf, C. Aisenbrey, N. Harmouche, J. Raya, P. Bertani, N. Voievoda, R. Suss, B. Bechinger, pH-dependent membrane interactions of the Histidine-rich cell-penetrating peptide LAH4-L1, Biophys. J. 113 (6) (2017) 1290–1300.
[19] Y. Nishimura, K. Takeda, R. Ezawa, J. Ishii, C. Ogino, A. Kondo, A display of pH-sensitive fusogenic GALA peptide facilitates endosomal escape from a bio-nanocapsule via an endocytic uptake pathway, J. Nanobiotechnology 12 (2014) 11–16.
[20] J.A. Kellum, M. Song, J. Li, Science review: extracellular acidosis and the immune response: clinical and physiologic implications, Crit. Care 8 (2004) 331–336.
[21] V. Estrella, T. Chen, M. Lloyd, J. Wojtkowiak, H.H. Cornnell, A. Ibrahim-Hashim, K. Bailey, Y. Balagurunathan, J.M. Rothberg, B.F. Sloane, J. Johnson, R.A. Gatenby, R.J. Gillies, Acidity generated by the tumor microenvironment drives local invasion, Cancer Res. 73 (2013) 1524–1535.
[22] I.F. Tannock, D. Rotin, Acid pH in tumors and its potential for therapeutic exploitation, Cancer Res. 49 (1989) 4373–4384.
[23] R.J. Gillies, Z. Liu, Z. Bhujwalla, 31P-MRS measurements of extracellular pH of tumors using 3-aminopropylphosphonate, Am. J. Phys. 267 (1994) C195–C203.
[24] R.A. Gatenby, R.J. Gillies, Why do cancers have high aerobic glycolysis? Nat. Rev. Cancer 4 (2004) 891–899.
[25] I. Ledaki, A. McIntyre, S. Wigfield, F. Buffa, S. McGowan, D. Baban, J.L. Li, A.L. Harris, Carbonic anhydrase IX induction defines a heterogeneous cancer cell response to hypoxia and mediates stem cell-like properties and sensitivity to HDAC inhibition, Oncotarget 6 (2015) 19413–19427.
[26] M. Anderson, A. Moshnikova, D.M. Engelman, Y.K. Reshetnyak, O.A. Andreev, Probe for the measurement of cell surface pH in vivo and ex vivo, Proc. Natl. Acad. Sci. U. S. A. 113 (2016) 8177–8181.
[27] M. Xu, X. Ma, T. Wei, Z.-X. Lu, B. Ren, In situ imaging of live-cell extracellular pH during cell apoptosis with surface-enhanced Raman spectroscopy, Anal. Chem. 90 (23) (2018) 13922–13928.

[28] J.C. Deacon, D.M. Engelman, F.N. Barrera, Targeting acidity in diseased tissues: mechanism and applications of the membrane-inserting peptide, pHLIP, Arch. Biochem. Biophys. 565C (2015) 40–48.
[29] C.J. Cheng, R. Bahal, I.A. Babar, Z. Pincus, F.N. Barrera, C. Liu, A. Svoronos, D.T. Braddock, P.M. Glazer, D.M. Engelman, W.M. Saltzman, F.J. Slack, MicroRNA silencing for cancer therapy targeted to the tumour microenvironment, Nature 518 (2015) 107–110.
[30] V.P. Nguyen, D.S. Alves, H.L. Scott, F.L. Davis, F.N. Barrera, A novel soluble peptide with pH-responsive membrane insertion, Biochemistry 56 (2015) 6567–6575.
[31] F.N. Barrera, D. Weerakkody, M. Anderson, O.A. Andreev, Y.K. Reshetnyak, D.M. Engelman, Roles of carboxyl groups in the transmembrane insertion of peptides, J. Mol. Biol. 413 (2011) 359–371.
[32] G.R. Grimsley, J.M. Scholtz, C.N. Pace, A summary of the measured pK values of the ionizable groups in folded proteins, Protein Sci.: A Publ. Protein Soc. 18 (2009) 247–251.
[33] L.C. Wyatt, A. Moshnikova, T. Crawford, D.M. Engelman, O.A. Andreev, Y.K. Reshetnyak, Peptides of pHLIP family for targeted intracellular and extracellular delivery of cargo molecules to tumors, Proc. Natl. Acad. Sci. U. S. A. 115 (2018) E2811–E2818.
[34] M. Werle, A. Bernkop-Schnurch, Strategies to improve plasma half life time of peptide and protein drugs, Amino Acids 30 (2006) 351–367.
[35] R. Galati, A. Verdina, G. Falasca, A. Chersi, Increased resistance of peptides to serum proteases by modification of their amino groups, Z. Naturforsch. 58c (2003) 558–561.
[36] P.E. Saw, S. Kim, I.-h. Lee, J. Park, M. Yu, J. Lee, J.-I. Kim, S. Jon, Aptide-conjugated liposome targeting tumor-associated fibronectin for glioma therapy, J. Mater. Chem. B 1 (2013) 4723–4726.
[37] J. Schindelin, I. Arganda-Carreras, E. Frise, V. Kaynig, M. Longair, T. Pietzsch, S. Preibisch, C. Rueden, S. Saalfeld, B. Schmid, J.Y. Tinevez, D.J. White, V. Hartenstein, K. Eliceiri, P. Tomancak, A. Cardona, Fiji: an open-source platform for biological-image analysis, Nat. Methods 9 (2012) 676–682.
[38] H.L. Scott, J.M. Westerfield, F.N. Barrera, Determination of the membrane translocation pK of the pH-low insertion peptide, Biophys. J. 113 (2017) 869–879.
[39] X. Zhang, D.S. Alves, J. Lou, S.D. Hill, F.N. Barrera, M.D. Best, Boronic acid liposomes for cellular delivery and content release driven by carbohydrate binding, Chem. Commun. 54 (2018) 6169–6172.
[40] S.H. White, W.C. Wimley, A.S. Ladokhin, K. Hristova, Protein folding in membranes: determining energetics of peptide-bilayer interactions, Methods Enzymol. 295 (1998) 62–87.
[41] A. Zorzi, S.J. Middendorp, J. Wilbs, K. Deyle, C. Heinis, Acylated heptapeptide binds albumin with high affinity and application as tag furnishes long-acting peptides, Nat. Commun. 8 (2017) 16092.
[42] A. Angelini, J. Morales-Sanfrutos, P. Diderich, S. Chen, C. Heinis, Bicyclization and tethering to albumin yields long-acting peptide antagonists, J. Med. Chem. 55 (2012) 10187–10197.
[43] J.S. Wall, E.B. Martin, T. Richey, A.C. Stuckey, S. Macy, C. Wooliver, A. Williams, J.S. Foster, P. McWilliams-Koeppen, E. Uberbacher, X. Cheng, S.J. Kennel, Preclinical validation of the heparin-reactive peptide p5+14 as a molecular imaging agent for visceral amyloidosis, Molecules 20 (2015) 7657–7682.
[44] J.S. Wall, T. Richey, A. Stuckey, R. Donnell, S. Macy, E.B. Martin, A. Williams, K. Higuchi, S.J. Kennel, In vivo molecular imaging of peripheral amyloidosis using heparin-binding peptides, Proc. Natl. Acad. Sci. U. S. A. 108 (2011) E586–E594.
[45] R.J. Gillies, N. Raghunand, M.L. Garcia-Martin, R.A. Gatenby, pH imaging. A review of pH measurement methods and applications in cancers, IEEE Engineering in Medicine and Biology Magazine: The Quarterly Magazine of the Engineering in Medicine & Biology Society, vol. 23, 2004, pp. 57–64.
[46] W.C. Wimley, Energetics of peptide and protein binding to lipid membranes, in: G. Anderluh, J. Lakey (Eds.), Proteins Membrane Binding and Pore Formation, Springer New York, New York, NY, 2010, pp. 14–23.
[47] H. Acar, J.M. Ting, S. Srivastava, J.L. LaBelle, M.V. Tirrell, Molecular engineering solutions for therapeutic peptide delivery, Chem. Soc. Rev. 46 (2017) 6553–6569.
[48] B.M. Elmadhoun, M.A. Swairjo, F.J. Burczynski, Fluorescent fatty acid transfer from bovine serum albumin to phospholipid vesicles: collision or diffusion mediated uptake, J. Pharm. Pharmaceut. Sci. 15 (2012) 420–432.
[49] S.D. Zucker, W. Goessling, J.L. Gollan, Kinetics of bilirubin transfer between serum albumin and membrane vesicles, J. Biol. Chem. 270 (1995) 1074–1081.
[50] J.M. Bergen, E.J. Kwon, T.W. Shen, S.H. Pun, Application of an environmentally sensitive Fluorophore for rapid analysis of the binding and internalization efficiency of gene carriers, Bioconjug. Chem. 19 (2008) 377–384.
[51] A.E. Johnson, Fluorescence approaches for determining protein conformations, interactions and mechanisms at membranes, Traffic (Copenhagen, Denmark) 6 (2005) 1078–1092.
[52] E.B. Martin, S.J. Kennel, T. Richey, C. Wooliver, D. Osborne, A. Williams, A. Stuckey, J.S. Wall, Dynamic PET and SPECT imaging with radioiodinated, amyloid-reactive peptide p5 in mice: a positive role for peptide dehalogenation, Peptides 60 (2014) 63–70.
[53] A. Tovar-Salazar, J. Dhawan, A. Lovejoy, Q.A. Liu, A.N. Gifford, Preparation of radioiodinated peptide nucleic acids with high specific activity, Anal. Biochem. 360 (2007) 92–98.
[54] E.B. Martin, A. Williams, T. Richey, C. Wooliver, A. Stuckey, J.S. Foster, S.J. Kennel, J.S. Wall, Evaluation of the effect of d-amino acid incorporation into amyloid-reactive peptides, J. Transl. Med. 15 (2017).
[55] F.A. Carone, D.R. Peterson, S. Oparil, T.N. Pullman, Renal tubular transport and catabolism of proteins and peptides, Kidney Int. 16 (1979) 271–278.
[56] J.-R. Oh, B.-C. Ahn, False-positive uptake on radioiodine whole-body scintigraphy: physiologic and pathologic variants unrelated to thyroid cancer, Am. J. Nucl. Med. Mol. Imaging 2 (2012) 362–385.
[57] G. Weaving, G.F. Batstone, R.G. Jones, Age and sex variation in serum albumin concentration: an observational study, Ann. Clin. Biochem. 53 (2016) 106–111.
[58] K. Baler, O.A. Martin, M.A. Carignano, G.A. Ameer, J.A. Vila, I. Szleifer, Electrostatic unfolding and interactions of albumin driven by pH changes: a molecular dynamics study, J. Phys. Chem. B 118 (2014) 921–930.
[59] E.M. Mazzaferro, E. Rudloff, R. Kirby, The role of albumin replacement in the critically ill veterinary patient, J. Vet. Emerg. Crit. Care 12 (2002) 113–124.
[60] R. Bottger, R. Hoffmann, D. Knappe, Differential stability of therapeutic peptides with different proteolytic cleavage sites in blood, plasma and serum, PLoS One 12 (2017) e0178943.
[61] R. Zou, X. Zhu, Y. Tu, J. Wu, M.P. Landry, Activity of antimicrobial peptide aggregates decreases with increased cell membrane embedding free energy cost, Biochemistry 57 (2018) 2606–2610.
[62] T.I. Rokitskaya, N.I. Kolodkin, E.A. Kotova, Y.N. Antonenko, Indolicidin action on membrane permeability: carrier mechanism versus pore formation, Biochim. Biophys. Acta 1808 (2011) 91–97.
[63] C.A. Castaneda, C.A. Fitch, A. Majumdar, V. Khangulov, J.L. Schlessman, B.E. Garcia-Moreno, Molecular determinants of the pKa values of Asp and Glu residues in staphylococcal nuclease, Proteins 77 (2009) 570–588.
[64] H. Hui, L. Farilla, P. Merkel, R. Perfetti, The short half-life of glucagon-like peptide-1 in plasma does not reflect its long-lasting beneficial effects, Eur. J. Endocrinol. 146 (2002) 863–869.
[65] M.J. Roberts, M.D. Bentley, J.M. Harris, Chemistry for peptide and protein PEGylation, Adv. Drug Deliv. Rev. 64 (2012) 116–127.
[66] M. Dharmalingam, U. Sriram, M.P. Baruah, Liraglutide: a review of its therapeutic use as a once daily GLP-1 analog for the management of type 2 diabetes mellitus, Indian J. Endocrinol. Metab. 15 (2011) 9–17.
[67] K. Chen, J. Xie, X. Chen, RGD-human serum albumin conjugates as efficient tumor targeting probes, Mol. Imaging 8 (2009) 65–73.
[68] M.S. Dennis, M. Zhang, Y.G. Meng, M. Kadkhodayan, D. Kirchhofer, D. Combs, L.A. Damico, Albumin binding as a general strategy for improving the pharmacokinetics of proteins, J. Biol. Chem. 277 (2002) 35035–35043.
[69] Y. Wang, A. Lomakin, S. Kanai, R. Alex, S. Belli, M. Donzelli, G.B. Benedek, The molecular basis for the prolonged blood circulation of lipidated incretin peptides: peptide oligomerization or binding to serum albumin? J. Control. Release 241 (2016) 25–33.
[70] D.C. Bode, H.F. Stanyon, T. Hirani, M.D. Baker, J. Nield, J.H. Viles, Serum Albumin's protective inhibition of amyloid-β fiber formation is suppressed by cholesterol, fatty acids and warfarin, J. Mol. Biol. 430 (2018) 919–934.
[71] P. Kurtzhals, S. Havelund, I. Jonassen, B. Kiehr, U.D. Larsen, U. Ribel, J. Markussen, Albumin binding of insulins acylated with fatty acids: characterization of the ligand-protein interaction and correlation between binding affinity and timing of the insulin effect in vivo, Biochem. J. 312 (1995) 725–731.
[72] M.T. Larsen, M. Kuhlmann, M.L. Hvam, K.A. Howard, Albumin-based drug delivery: harnessing nature to cure disease, Mol. Cell. Ther. 4 (2016) 3.
[73] I. Petitpas, A.A. Bhattacharya, S. Twine, M. East, S. Curry, Crystal structure analysis of warfarin binding to human serum albumin: anatomy of drug site I, J. Biol. Chem. 276 (2001) 22804–22809.
[74] N.E. Basken, C.J. Mathias, M.A. Green, Elucidation of the human serum albumin (HSA) binding site for the Cu-PTSM and Cu-ATSM radiopharmaceuticals, J. Pharm. Sci. 98 (2009) 2170–2179.
[75] G. Fanali, Y. Cao, P. Ascenzi, V. Trezza, T. Rubino, D. Parolaro, M. Fasano, Binding of delta9-tetrahydrocannabinol and diazepam to human serum albumin, IUBMB Life 63 (2011) 446–451.
[76] I. Jonassen, S. Havelund, T. Hoeg-Jensen, D.B. Steensgaard, P.-O. Wahlund, U. Ribel, Design of the novel protraction mechanism of insulin Degludec, an ultra-long-acting basal insulin, Pharm. Res. 29 (2012) 2104–2114.
[77] C. Tassa, J.L. Duffner, T.A. Lewis, R. Weissleder, S.L. Schreiber, A.N. Koehler, S.Y. Shaw, Binding affinity and kinetic analysis of targeted small molecule-modified nanoparticles, Bioconjug. Chem. 21 (2010) 14–19.
[78] R. Thakur, A. Das, A. Chakraborty, Interaction of human serum albumin with liposomes of saturated and unsaturated lipids with different phase transition temperatures: a spectroscopic investigation by membrane probe PRODAN, RSC Adv. 4 (2014) 14335–14347.
[79] D. Charbonneau, M. Beauregard, H.-A. Tajmir-Riahi, Structural analysis of human serum albumin complexes with cationic lipids, J. Phys. Chem. B 113 (2009) 1777–1784.
[80] M.N. Dimitrova, H. Matsumura, A. Dimitrova, V.Z. Neitchev, Interaction of albumins from different species with phospholipid liposomes. Multiple binding sites system, Int. J. Biol. Macromol. 27 (2000) 187–194.
[81] J.A. Cohlberg, Km as an apparent dissociation constant, J. Chem. Educ. 56 (1979) 512.
[82] A. Senes, D.E. Engel, W.F. DeGrado, Folding of helical membrane proteins: the role of polar, GxxxG-like and proline motifs, Curr.Opin.Struct.Biol. 14 (2004) 465–479.
[83] W.P. Russ, D.M. Engelman, The GxxxG motif: a framework for transmembrane helix-helix association, J.Mol.Biol. 296 (2000) 911–919.
[84] L. Treuel, D. Docter, M. Maskos, R.H. Stauber, Protein corona - from molecular adsorption to physiological complexity, Beilstein J Nanotechnol 6 (2015) 857–873.
[85] M.P. Monopoli, C. Aberg, A. Salvati, K.A. Dawson, Biomolecular coronas provide the biological identity of nanosized materials, Nat. Nanotechnol. 7 (2012) 779–786.